Optical rogue-wave patterns in coupled defocusing systems

Yan-Hong Qin [1,2] Liming Ling [3,*] and Li-Chen Zhao [4,5,6,†]

[1] *College of Mathematics and System Sciences, Xinjiang University, Urumqi 830046, China*
[2] *Institute of Mathematics and Physics, Xinjiang University, Urumqi 830046, China*
[3] *School of Mathematics, South China University of Technology, Guangzhou 510640, China*
[4] *School of Physics, Northwest University, Xi'an 710127, China*
[5] *Shaanxi Key Laboratory for Theoretical Physics Frontiers, Xi'an 710127, China*
[6] *Peng Huanwu Center for Fundamental Theory, Xi'an 710127, China*

(Received 11 December 2022; revised 11 July 2023; accepted 3 August 2023; published 21 August 2023)

We systematically investigate the spatial-temporal patterns of rogue waves in N-component coupled defocusing nonlinear Schrödinger equations where $N \geqslant 2$. The fundamental rogue-wave solutions are given in a unified form for both focusing and defocusing cases. We establish the quantitative correspondence between modulation instability and rogue-wave patterns, which develops the previously reported inequality relation into an equation correspondence. As an example, we demonstrate phase diagrams for rogue-wave patterns in a two-component coupled system, based on the complete classification of their spatial-temporal structures. The phase diagrams enable us to predict various rogue-wave patterns, such as the ones with a four-petaled structure in both components. These results are meaningful for controlling the rogue-wave excitations in two orthogonal polarization optical fibers.

DOI: 10.1103/PhysRevA.108.023519

I. INTRODUCTION

Optical systems provide a good platform for studying rogue waves (RWs) [1–3], which could endanger marine navigation and optical communications. Some rational solutions of N-component nonlinear Schrödinger equations (NLSEs) have been widely used to describe RW phenomena in nonlinear optics fibers with taking no higher-order effects [3,4], and other nonlinear systems [5–10]. In most previous studies, RW solutions were obtained in focusing NLSEs [10–19]. The fundamental RW for a scalar NLSE ($N = 1$) is always eye-shaped (ES) [4]. However, vector RWs ($N \geqslant 2$) can involve an eye-shaped one [14,15], an anti-eye-shaped (AES) one [16], and a four-petaled (FP) one [17], since vector systems allow for energy transfer between the coupled waves. The nonlinear superposition of these fundamental RWs can produce more diverse structures, which refer to the higher-order RWs or multiple RWs [20–24]. So far, modulation instability (MI) is believed to play an important role in RWs' excitations [25–29]. Moreover, the equation correspondence between the fundamental RW solution and the dispersion relation of MI was established in the focusing N-component NLSE [30], which can be used to interpret the RW patterns perfectly. It predicts that there are mainly three different pattern types for arbitrary N-component coupled focusing NLSEs in integrable cases.

In contrast, RWs cannot exist in the scalar defocusing NLSE, since there is no MI on the plane wave background. Several recent pieces of literature have reported the existence of vector RWs in integrable two-component defocusing systems [31–35], subject to certain constraints on the two plane wave backgrounds. Those theoretical results have motivated experiments to observe AES-AES (i.e., dark-dark) RWs in nonlinear optical fibers [36,37]. AES-AES RW refers to the two components admitting the AES RW pattern. However, the classification of vector RW patterns is still unclear, let alone the N-component case where $N > 2$. On the other hand, an inequality relation between the RW solutions and MI was suggested [31], which inspired many discussions about the generation mechanism of RWs [28,30,38]. It is very essential to establish the equation correspondence between MI and RWs' spatial-temporal structures for defocusing cases, which is also meaningful for controllably exciting various vector RWs in experiments.

In this paper, we systematically study the patterns of vector RWs in coupled defocusing nonlinear systems, based on the general exact RW solutions of N-component defocusing NLSEs where $N \geqslant 2$. Importantly, we successfully establish the equation correspondence between MI and RW solutions, which provides the quantitative mechanism of vector RWs in the defocusing regime. For example, we present phase diagrams to illustrate the families of two-component RWs in defocusing and focusing regimes. FP-FP patterns are predicted based on the phase diagrams, in contrast to the previously observed AES-AES RW [36,37]. We further discuss the possibility of experimentally observing them from weakly localized perturbations in two orthogonal polarization optical fibers.

The paper is organized as follows. In Sec. II, we first present the unified RW solutions in arbitrarily N-component

*linglm@scut.edu.cn
†zhaolichen3@nwu.edu.cn

coupled NLSEs in both defocusing and focusing regimes, where $N \geqslant 2$. Then, the systematic classification of vector RWs in the two-component case is demonstrated clearly, by giving three sets of phase diagrams for RW patterns. In Sec. III, we obtain the equation correspondence between the dispersion relation of MI and the existing condition of RW patterns, which implies that the resonance perturbations in MI regions can be used to generate RW controllably and directly. In Sec. IV, we discuss the possibilities of observing vector RW patterns in defocusing nonlinear fibers. For example, numerical simulations demonstrate that FP-FP RWs can be excited perfectly by combining the phase diagrams and using the resonance perturbations. Finally, we summarize our results in Sec. V.

II. ROGUE-WAVE PATTERNS IN COUPLED NONLINEAR SCHRÖDINGER SYSTEMS

A. The unified vector rogue-wave solutions

The propagation of nonlinear waves through optical fiber arrays has been found to be governed by a set of equations that are related to the coupled NLSEs [39–43]:

$$i\mathbf{\Phi}_{\xi} + \tfrac{1}{2}\mathbf{\Phi}_{\tau\tau} + \sigma\mathbf{\Phi}\mathbf{\Phi}^{\dagger}\mathbf{\Phi} = 0, \tag{1}$$

where $\mathbf{\Phi} = (\phi_1, \phi_2, \ldots, \phi_N)^{\mathrm{T}}$. The symbols T and † represent transpose and Hermite conjugation of a matrix, respectively. For arbitrary N, Eq. (1) can govern the propagation of N self-trapped mutually incoherent wave packets in Kerr-like photorefractive media [39,41,43], and ξ and τ represent the normalized distance along the fiber and the retarded time, respectively. $\phi_i(\tau, \xi)$ represents the complex slowly varying envelope of the ith component. Here, $\sigma = 1$ and $\sigma = -1$ correspond to focusing and defocusing nonlinearities, respectively. In the case of focusing, RW solutions have been systematically obtained for arbitrary N [30]. However, in the defocusing case, the analytical vector RW solution has recently been derived for $N = 2$, giving AES-AES RWs and AES-ES (i.e., dark-bright) RWs [31,32]. In this section, we intend to present exact RW solutions that, as will be demonstrated, can be derived for a general value of N (where $N \geqslant 2$) in Eq. (1) with $\sigma = -1$.

To obtain the RW solution of an N-component coupled NLSE model, a crucial step is to find multiple roots of a high-order polynomial [an $(N+1)$th order algebraic equation] with respect to the spectral parameter. This aspect makes it challenging to solve the polynomial directly, and it is hard to obtain the analytical solution for RWs. In this paper, we propose an innovative idea to solve the problems. Technically, we expand the Lax pair spectrum curve at branch points to derive the determining equation for obtaining double roots of the RW solutions, instead of directly solving the high-order polynomial. By following the Darboux transformation method [21,23] with the aid of the expanding technique, we obtain a concise and unified expression for the vector RW solution of the N-component NLSE in the defocusing regime

$$\phi_i = a_i\left\{1 + \frac{2i(\chi_R + b_i)(\tau + \chi_R\xi) - 2i\chi_I^2\xi - 1}{\varpi_i\left[(\tau + \chi_R\xi)^2 + \chi_I^2\xi^2 + 1/\left(4\chi_I^2\right)\right]}\right\}e^{i\theta_i}. \tag{2}$$

Surprisingly, the form of this solution is identical to that of the well-known focusing regime [30]. Here, $\varpi_i = (\chi_R + b_i)^2 + \chi_I^2$, $\theta_i = b_i\tau + (\sigma\sum_{i=1}^{N} a_i^2 - \frac{b_i^2}{2})\xi$, and $i = 1, 2, \ldots, N$. The parameters a_i and b_i represent the amplitude and frequency of the background, respectively, in the ith component. The velocity of the vector RW can be obtained directly and exactly from this solution as $v = -\chi_R$. In Eq. (2), $\chi_R = \mathrm{Re}(\chi)$, $\chi_I = \mathrm{Im}(\chi)$, and χ is a complex root of the following algebraic equation:

$$1 + \sigma\sum_{i=1}^{N}\frac{a_i^2}{(\chi + b_i)^2} = 0, \tag{3}$$

which is the determining equation for RW solutions. For the focusing case ($\sigma = 1$), the above algebraic equation is positive definite and always admits N pairs of complex conjugate roots [30]. In contrast, this polynomial is non-positive-definite in the defocusing regime ($\sigma = -1$), which confirms the existence of at least two real roots; namely, Eq. (3) admits $N - 1$ pairs of complex conjugate roots at most. Naturally, RW solutions cannot be allowed in scalar-defocusing cases. Therefore, to obtain RW solutions in the defocusing case, the amplitudes and frequencies of the vector background must be strictly and adequately designed to get a complex root of χ, instead of being free parameters in the focusing cases.

Some RW solutions have been presented in two-component defocusing nonlinear systems [31–35], such as AES-ES RW and AES-AES RW. However, in the defocusing case, the classification of RW patterns has yet to be thoroughly investigated, and the parameter domains for different vector RWs have not been analyzed. The fundamental RW patterns in the focusing case had been studied clearly, mainly including the ES, AES, and FP ones [30]. As such, we will further explore the distinction and connection between vector RWs in the focusing and defocusing cases. Then, we will conduct a systematic investigation of the pattern classification of fundamental vector RWs in the two-component case as an example.

B. The pattern classification of fundamental vector rogue waves

In the defocusing regime with $N = 2$, we get that the discriminant to the existence of RW is $[a_1^2 + a_2^2 - (b_1 - b_2)^2]^3 + 27a_1^2a_2^2(b_1 - b_2)^2 > 0$, which ensures the presence of a pair of complex conjugate roots of Eq. (3). Without loss of generality, we present the phase diagrams of vector RW solutions in Fig. 1(a) setting $a_2 = 1$ and $b_2 = -b_1$. We denote the paired complex conjugate roots that satisfy the discriminant as χ_1. The RW cannot be excited in the parameter space marked by the white regions and white lines in the (b_1, a_1) plane. The critical condition for RW nonexcitation, depicted by the black dashed curves, is calculated as $a_1 = [3(4b_1^2)^{\frac{1}{3}} - 3(4b_1^2)^{\frac{2}{3}} + 4b_1^2 - 1]^{1/2}$. The critical lines mean the disappearance of a pair of conjugate complex roots of the branch equation (3), which results in two identical real roots. By analyzing the extreme points of RW solutions, we get that the solutions (2) with $\frac{(\chi_R+b_i)^2}{\chi_I^2} \leqslant \frac{1}{3}$, $\frac{1}{3} < \frac{(\chi_R+b_i)^2}{\chi_I^2} < 3$, and $\frac{(\chi_R+b_i)^2}{\chi_I^2} \geqslant 3$ can form the ES RW (pink areas), FP RW (green areas), and AES RW (blue areas), respectively. The boundaries of various

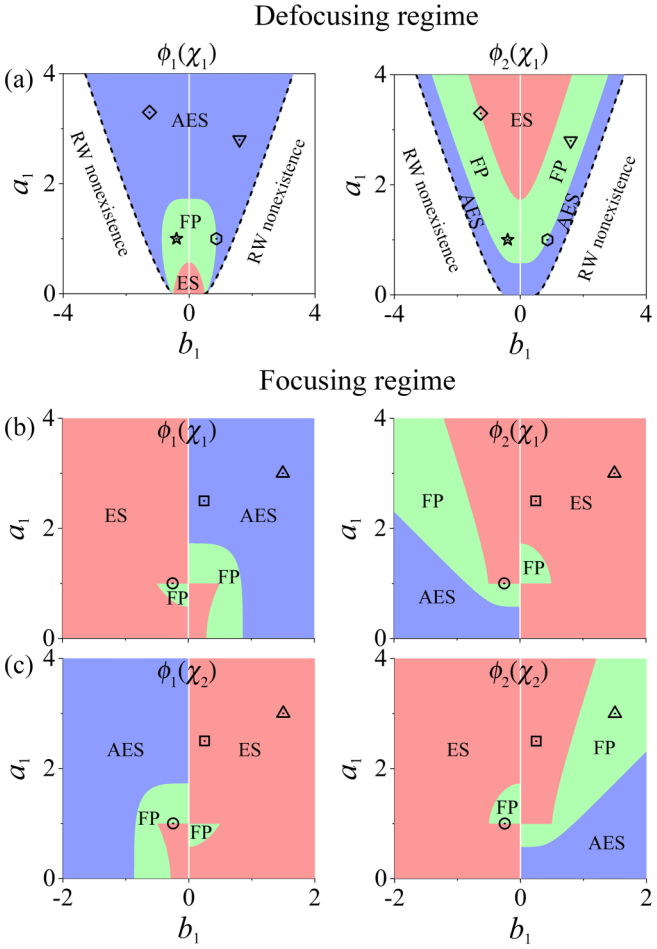

FIG. 1. The phase diagrams for patterns of two-component vector RWs in the (b_1, a_1) plane. The pink, green, and blue regions denote the RW solutions with ES, FP, and AES patterns. (a) Defocusing case. The white regions and white lines ($b_1 = 0$) denote RW nonexistence. Black dashed curves depict the critical conditions of RW nonexcitations. Examples of the family of vector RWs are shown in Figs. 2(a)–2(d). The parameters for each type of RW are denoted by a specific symbol: a hexagon ($b_1 = \sqrt{3}/2, a_1 = 1$), a diamond ($b_1 = -1.25799, a_1 = 3.2983$), an inverted triangle ($b_1 = 1.6, a_1 = 2.8$), and a star ($b_1 = -0.4, a_1 = 1$). (b) and (c) Two sets of phase diagrams depicting the patterns of vector RWs in the focusing regime. As examples, three sets of intensity profiles for vector RWs are shown in Fig. 3. The parameters for each set of profiles in Figs. 3(a1) and 3(a2), 3(b1) and 3(b2), and 3(c1) and 3(c2) are indicated by triangle ($b_1 = 3/2, a_1 = 3$), square ($b_1 = 1/4, a_1 = 5/2$), and circle ($b_1 = -1/4, a_1 = 1$) symbols, respectively. Other parameters are $a_2 = 1$ and $b_2 = -b_1$.

regions are obtained by parameters that satisfy $\frac{(\chi_R+b_i)^2}{\chi_I^2} = \frac{1}{3}$ or $\frac{(\chi_R+b_i)^2}{\chi_I^2} = 3$.

The phase diagrams in Fig. 1(a) demonstrate that the family of vector RWs in the defocusing cases includes AES-ES RW, AES-FP RW, AES-AES RW, and FP-FP RW. Here, AES-ES RW and ES-AES RW are considered to be the same vector RW, and the definitions of the other vector RWs are similar to this case. In Ref. [31], only the AES-AES RW and AES-ES RW were obtained in the defocusing regime. Figure 1(a) also

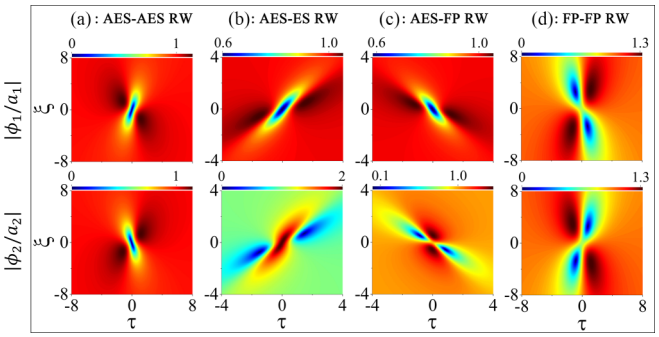

FIG. 2. The intensity profiles of four fundamental types of vector RWs in the two-component defocusing regime, normalized to their respective backgrounds. The top (bottom) row corresponds to the intensity profiles of the first (second) component. The parameters associated with each type of vector RWs correspond to the symbols shown in Fig. 1(a), namely, a hexagon, a diamond, an inverted triangle, and a star for (a), (b), (c), and (d), respectively.

indicates that ES-ES RW and ES-FP RW are not allowed in the defocusing regime. Examples of solution profiles for the RW family are shown in Fig. 2. The symbols shown in Fig. 1(a), namely, a hexagon, a diamond, an inverted triangle, and a star, correspond to the parameters associated with each type of vector RWs in Figs. 2(a), 2(b), 2(c), and 2(d), respectively. The parameters for the diamond ($\frac{(\chi_R+b_2)^2}{\chi_I^2} = \frac{1}{3}$) and the hexagon ($\frac{(\chi_R+b_1)^2}{\chi_I^2} = 3$ and $\frac{(\chi_R+b_2)^2}{\chi_I^2} = 3$) are set at the boundaries of the pink and blue regions, respectively, among these symbols. There is no difference in the dynamical behavior of RWs at the boundaries or within the different regions. The phase diagram Fig. 1(a) also demonstrates that the probability of forming AES RW far outweighs that of ES RW and FP RW in the component ϕ_1. When the amplitude $a_1 > 1.73$, the component ϕ_1 only allows the AES RW. In contrast, the probability of exciting ES RW and FP RW in the component ϕ_2 is much greater than that of exciting AES RW. Remarkably, the FP-FP RW can be produced in a small parameter domain in regions with amplitude $a_1 \in [0.58, 1.73]$. This phase diagram clearly demonstrates the existence conditions of vector RW solutions and the classification of RW patterns in defocusing two-component systems, which has never been determined in previous works. Similar phase diagrams can be obtained by taking other parameters.

In contrast, in the focusing regime, there are no restrictions on the amplitudes and frequencies of the vector background for the excitations of vector RWs. In this case, Eq. (3) always produces two pairs of complex conjugate roots, denoted as χ_1 and χ_2, resulting in two distinct sets of phase diagrams, as depicted in Figs. 1(b) and 1(c). As illustrated, the RW patterns can be always excited in the (b_1, a_1) plane, and these RW patterns comprise ES-ES RW, ES-FP RW, ES-AES RW, and FP-FP RW. Therefore both ES-AES RW and FP-FP RW can exist in both the focusing and defocusing regimes. Strikingly, the FP-FP RW only can be generated in a small parameter space characterized by the two small green fan-shaped areas. More interestingly, in most cases, the types of vector RWs in the case of χ_1 are distinct from those in χ_2 for identical values of a_i and b_i, rather than a mere exchange of RW types between

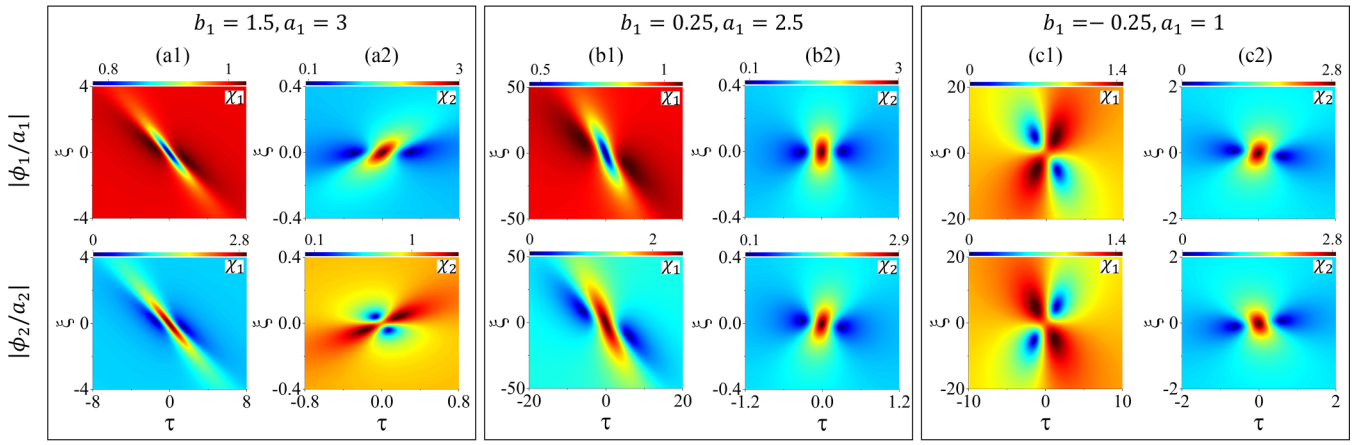

FIG. 3. Examples of three sets of vector RWs in the focusing regime, with each set containing two different types of vector RWs on the same vector background. In (a1) and (a2), (b1) and (b2), and (c1) and (c2), the parameters correspond to the triangle, square, and circle symbols, respectively, depicted in Figs. 1(b) and 1(c).

two components. This is not possible in the defocusing case. In Ref. [44], only a phase diagram similar to Fig. 1(c) was presented, where the parameter regions for FP-FP RW had been lost. For instance, in Fig. 3, we present three sets of vector RWs corresponding to three distinct vector backgrounds. Each set includes two different types of vector RWs excited on the same vector background. Figures 3(a1) and 3(a2) present AES-ES RW for χ_1 and ES-FP RW for χ_2, with parameters corresponding to the triangle symbol in Figs. 1(b) and 1(c). AES-ES RW and ES-ES RW are observed in Figs. 3(b1) and 3(b2), with the parameters matching the square symbol in Figs. 1(b) and 1(c). In each of these two sets, the evolution velocities of these two types have equal values but opposite directions. Additionally, Figs. 3(c1) and 3(c2) present the existence of FP-FP RW for χ_1 and ES-ES RW for χ_2, with parameters corresponding to the circle symbol in Figs. 1(b) and 1(c). By directly calculating χ_R (i.e., $\chi_{1,R}$ and $\chi_{2,R}$) from Eq. (3), we have determined that their velocities remain static, which cannot be observed from the intensity profiles. The succinct RW solution (2) and determinant equation (3) help us understand the dynamical characteristics of vector RWs much more directly and accurately.

III. THE EQUATION CORRESPONDENCE BETWEEN MODULATION INSTABILITY AND ROGUE-WAVE PATTERNS

Previous studies suggested that baseband MI can be seen as the origin for RW formations in the defocusing nonlinear regime [31,38]. However, the correspondence relation between the RW existence condition and baseband MI was an inequality form, which was also obtained in the two-component case. In the defocusing case, the quantitative correspondence between the MI and the existing condition of RW solutions is still lacking. The equation correspondence for the focusing N-component NLSE [30] motivates us to look further for similar results for defocusing cases.

We revisit the standard MI analysis. The linearized stability of perturbations on the plane wave solution can be obtained by adding weak perturbations with Fourier modes. Then, a perturbed vector background is written as

$$\phi_i = \phi_i^{[0]}[1 + p_i(\tau, \xi)], \quad i = 1, 2, \ldots, N. \tag{4}$$

Here, $\phi_i^{[0]} = a_i \exp(i\theta_i)$ are vector background solutions, and $p_i(\tau, \xi)$ are small perturbations which satisfy the linear equation

$$i(p_{i,\xi} + b_i p_{i,\tau}) + \frac{1}{2} p_{i,\tau\tau} + \sigma \sum_{l=1}^{N} \left[a_l^2 (p_l + p_l^*)\right] = 0. \tag{5}$$

The asterisk means complex conjugate. We suppose the perturbations $p_i(\tau, \xi)$ have the form

$$p_i(\tau, \xi) = p_{i,-k}^* e^{-i\mu_k(\tau + \Omega_k^* \xi)} + p_{i,k} e^{i\mu_k(\tau + \Omega_k \xi)}. \tag{6}$$

Substituting $p_i(\tau, \xi)$ into the linearized equation (5), we get following linear homogeneous equations:

$$\mathcal{K}\mathcal{P} = 0. \tag{7}$$

Here, coefficient matrix $\mathcal{K}$ is

$$\mathcal{K} = \mathrm{diag}\Big[\big(-\Omega_k - b_1 - \tfrac{1}{2}\mu_k\big)\mu_k, \big(\Omega_k + b_1 - \tfrac{1}{2}\mu_k\big)\mu_k, \cdots, \big(-\Omega_k - b_N - \tfrac{1}{2}\mu_k\big)\mu_k, \big(\Omega_k + b_N - \tfrac{1}{2}\mu_k\big)\mu_k\Big] + \sigma\mathcal{A},$$

$$\mathcal{A} = \begin{pmatrix} a_1^2 & a_1^2 & \cdots & a_N^2 & a_N^2 \\ \vdots & \vdots & \vdots & \vdots & \vdots \\ a_1^2 & a_1^2 & \cdots & a_N^2 & a_N^2 \end{pmatrix}.$$

$\mathcal{A}$ is a $2N \times 2N$ matrix. The determinant of matrix $\mathcal{K}$ is

$$\det(\mathcal{K}) = \mu_k^{2N} \prod_{l=1}^{N} \left[\frac{1}{4}\mu_k^2 - (\Omega_k + b_l)^2\right] \times \left[1 + \sigma \sum_{l=1}^{N} \frac{a_l^2}{(\Omega_k + b_l)^2 - \frac{1}{4}\mu_k^2}\right]. \tag{8}$$

To get the nonzero solution of vector $\mathcal{P}$, the determinant $\det(\mathcal{K})$ must be equal to zero, which is the dispersion relation for linearized disturbance, i.e., $1 + \sigma \sum_{l=1}^{N} \frac{a_l^2}{(\Omega_k + b_l)^2 - \frac{1}{4}\mu_k^2} = 0$. The roots Ω_k with a nonzero imaginary part correspond to linearly unstable modes, with growth rate $|\mathrm{Im}(\mu_k \Omega_k)|$.

The corresponding nonzero eigenvector $\mathcal{P}$ associated with an eigenvalue Ω is given by

$$\mathcal{P} = \begin{pmatrix} p_{1,k} \\ p_{1,-k} \\ \vdots \\ p_{N,k} \\ p_{N,-k} \end{pmatrix} = c \begin{pmatrix} (\mu_k + 2b_1 + 2\Omega)^{-1} \\ (\mu_k - 2b_1 - 2\Omega)^{-1} \\ \cdots \\ (\mu_k + 2b_N + 2\Omega)^{-1} \\ (\mu_k - 2b_N - 2\Omega)^{-1} \end{pmatrix},$$

where c is a nonzero complex number. It was suggested that RWs came from the resonance perturbations in MI regions [28,29], which refers to the fact that both the dominant frequency and the propagation constant of perturbation are equal to those of the background. Inspired by this, we take the limit $\mu_k \to 0$ to address the dispersion relation of MI in the defocusing case, which can be expressed as

$$1 + \sigma \sum_{l=1}^{N} \frac{a_l^2}{(\Omega_k + b_l)^2} = 0. \tag{9}$$

Surprisingly, this MI dispersion relation form is consistent with the determining equation (3) of RW solutions, which means the equation correspondence between the two (i.e., $\chi = \Omega_k$). $\mathrm{Re}(\Omega_k)$ stands for the evolution energy of the perturbation, and $\mathrm{Im}(\Omega_k)$ denotes the growth rate of a perturbation responsible for the formation of RWs. The above dispersion relation with $\sigma = -1$ is non-positive-definite, which leads to two types of dispersion relations. One is $\mathrm{Im}(\Omega_k) \equiv 0$, which stands for the linearly stable mode [denoted as the modulational stability (MS) branch]. However, the other can admit $\mathrm{Im}(\Omega_k) \neq 0$ under some special constraints on the amplitudes and frequencies of the background, which corresponds to the linearly unstable mode (denoted as the MI branch). Therefore only if the weak perturbations are set in the MI branch can the RWs be excited, as in the phase diagram shown in Fig. 1(a). Then, based on the equation correspondence between the MI and RW solution, i.e., $\chi = \Omega_k$, the RW patterns evolved from the MI branch can be predicted. However, when the weak perturbations choose the MS branch, the dynamical evolutions could produce vector dark solitons on the plane wave background [45,46]. For example, when $N = 1$ with $\sigma = -1$, it is easy to get $\Omega_k = \pm a_1 - b_1$. Therefore only the MS branch exists in scalar defocusing nonlinear systems, which admit dark solitons rather than RWs [46,47]. For two-component defocusing systems, both the MS and MI branches can exist, so dark solitons can coexist with RWs or breathers [34].

For the focusing case, i.e., $\sigma = 1$, the above dispersion relation equation (9) is positive definite, which leads to the roots Ω_k with a nonzero imaginary part. Therefore there are always N MI branches in the N-component cases. By choosing any one of the MI branches, the RW patterns can be generated from the localized perturbation in the background. Meanwhile, different RW patterns can be excited on the same background for vector cases, because of the existence of multiple MI branches, as in the example shown in Figs. 1(b), 1(c), and 3. The N-component focusing system can possess N different patterns in each component at most. In contrast, in the defocusing case, each component can admit $N - 1$ different RW patterns at most in an N-component system.

Equations (3) and (9) have confirmed that the quantitative correspondence between the MI and RW solutions exists in both the defocusing and focusing nonlinear systems, which develops the previously reported inequality relation [31] into an equation correspondence. It indicates that the RW patterns can be excited conveniently and controllably by using the weak resonance perturbations in MI regions.

IV. THE POSSIBILITIES OF OBSERVING VECTOR ROGUE-WAVE PATTERNS IN DEFOCUSING NONLINEAR FIBERS

The above theoretical results can be used to excite vector RWs in a controllable way. The phase diagram in Fig. 1(a) guides one to design the amplitudes and frequencies of the two plane wave backgrounds for generating a certain RW pattern. The equation correspondence between MI and RWs indicates that the resonance perturbations in the MI regions can be used to generate RWs conveniently. Namely, we can excite RWs by adding an arbitrary localized perturbation instead of approaching the ideal initial condition given by the exact solution.

Recently, optical dark-dark RWs have been observed experimentally [36,37] in two orthogonally polarized optical fibers [48]. We set the parameter settings to be identical to Ref. [36] to discuss the possibilities of experimentally exciting other types of vector RWs in the two-component defocusing case. The propagation of two orthogonally polarized optical pump waves at a relative frequency offset Δ in a random weakly birefringent telecom fiber is described by the dimensional Manakov equations, $i\Phi_{1,z} + i\delta/2\Phi_{1,t} - \beta_2/2\Phi_{1,tt} + \gamma(|\Phi_1|^2 + |\Phi_2|^2)\Phi_1 = 0$ and $i\Phi_{2,z} - i\delta/2\Phi_{2,t} - \beta_2/2\Phi_{2,tt} + \gamma(|\Phi_1|^2 + |\Phi_2|^2)\Phi_2 = 0$. Here, z and t denote the dimensional propagation distance and retarded time coordinates, respectively. Φ_1 (Φ_2) is a slow (fast) wave. $\delta = \beta_2\Delta$ is associated with their group-velocity mismatch owing to normal group-velocity dispersion. β_2 and γ are the group-velocity dispersion and the effective Kerr nonlinear coefficient, respectively. There is a transformation between the dimensional and dimensionless models, i.e., $\Phi_1(t,z) = \sqrt{P_0}\phi_1 \exp(i\frac{\delta}{2\beta 2}t - i\frac{\delta^2}{8\beta 2}z)$, $\Phi_2(t,z) = \sqrt{P_0}\phi_2 \exp(-i\frac{\delta}{2\beta 2}t - i\frac{\delta^2}{8\beta 2}z)$, $t = -\tau t_0$, $z = \xi z_0$, with $z_0 = (\gamma P_0)^{-1}$, and $t_0 = \sqrt{\beta_2 z_0}$. Referring to the experiments [36,37,48], the optical fiber can be a reverse-TrueWave fiber with a chromatic dispersion of $-14\,\mathrm{ps\,nm^{-1}\,km^{-1}}$ (equivalent to $\beta_2 = 18\,\mathrm{ps^2/km}$), a nonlinear coefficient $\gamma = 2.4\,\mathrm{W^{-1}\,km^{-1}}$, and an attenuation of 0.25 dB/km at the central wavelength $\lambda_0 = 1554.7\,\mathrm{nm}$. $P_0 = \frac{9\pi^2\Delta^2\beta_2}{8\gamma}$ denotes the power for which the low cutoff frequency vanishes. The frequency detuning Δ can range from 50 to 500 GHz at λ_0. In the following discussion, we choose $\Delta = 300\,\mathrm{GHz}$. Then, $P_0 = 7.4947\,\mathrm{W}$, the nonlinear length is $z_0 = 0.0556\,\mathrm{km}$, and the timescale is $t_0 = 1\,\mathrm{ps}$.

The phase diagram in Fig. 1(a) reveals that the FP-FP RW is predominantly observed in regions with amplitudes $a_1 \in [0.58, 1.73]$ and $a_2 = 1$ and frequencies $b_1 \in [-0.76, 0.76]$ and $b_2 = -b_1$ for the vector background. For example, we select the parameters indicated by star symbol shown in Fig. 1 to create FP-FP RW expectantly. We first

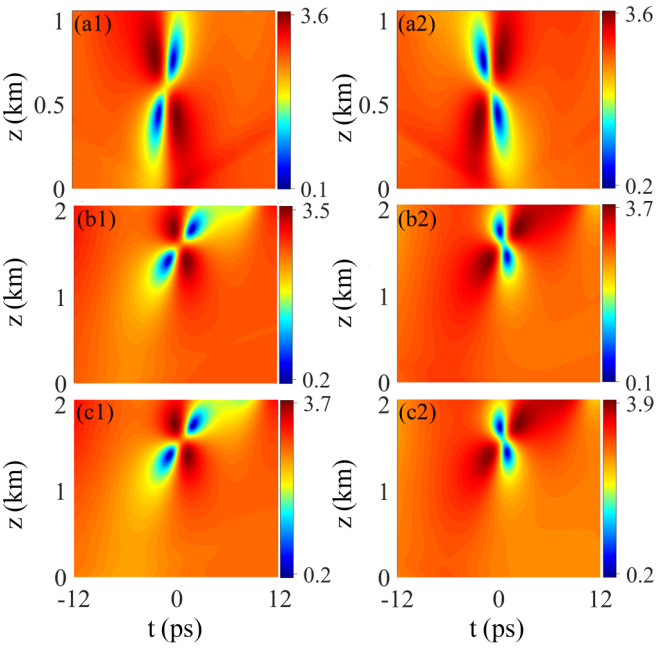

FIG. 4. Optical intensities in two orthogonal polarization waves [$|\Phi_1(t,z)|$ (left) and $|\Phi_2(t,z)|$ (right)], describing the numerical excitation of optical FP-FP RW. (a1) and (a2) The initial conditions given by an exact solution with Gaussian white noise and parameter deviation of χ. (b1) and (b2) Numerical evolution from a plane wave background perturbed by a weak Gaussian pulse perturbation. (c1) and (c2) Numerical evolution from a plane wave background perturbed by a weak Gaussian pulse perturbation, taking into account the effects of third-order dispersion and fiber loss. The parameters of the vector background correspond to the star symbol in Fig. 1.

consider the numerical evolutions from the initial condition given by the exact solution (2) with the parameter deviation and adding Gaussian white noise. We set $\Phi_{j,\text{noise}}(t,0) = \Phi_j(t,-9;\chi)[1+\text{rand}(1)/10\times\exp(-t^2/4)]$ $(j=1,2)$ and $\chi = \chi_1 + \text{rand}(1)/20$, where rand(1) is random complex numbers with norm less than 1, and $\chi_1 = 0.3473i$ is determined by Eq. (3). The simulation results presented in Figs. 4(a1) and 4(a2) display the typical FP-FP RW patterns, which are consistent with the exact results shown in Fig. 2(d). However, it is inconvenient to prepare such ideal initial states in real experiments.

Importantly, the equation correspondence between MI and RWs indicates that the resonance perturbations in the MI regions can be conveniently used to generate RWs. This means that we can excite RWs by adding an arbitrary localized perturbation, instead of approaching the ideal initial condition provided by the exact solution. Therefore, for example, we conduct numerical simulations to generate FP-FP patterns, by adding a weak Gaussian pulse perturbation on the vector background [24,28]. Namely, $\Phi_j(t,0) = a_j\exp(i\theta_j)\sqrt{P_0}\{1+\varepsilon_j\exp[-\frac{(t-\delta_j)^2}{w_j^2}]\}$ $(j=1,2)$, where ε_j, δ_j, and w_j denote the amplitude, offset, and width of perturbation in the ith mode, respectively. We illustrate the numerical evolutions in Figs. 4(b1) and 4(b2) by choosing $\varepsilon_1 = -\varepsilon_2 = -0.1$, $w_1 = w_2 = 5$, and $\delta_1 = \delta_2 = -6$ and using the same vector background as in Figs. 4(a1) and 4(a2). As predicted in the phase diagrams in Fig. 1(a), the FP-FP RW emerges quickly and successfully at a propagation distance of approximately $z \approx 1.2$ km, which is in contrast to the previously observed dark-dark RWs reported in the literature [36,37]. As observed in Figs. 4(b1) and 4(b2), the temporal-spatial structures excited by the localized perturbation in the MI region exhibit good agreement with the patterns shown in Fig. 2(d), provided by the exact analytical solution, and Figs. 4(a1) and 4(a2), which evolves from the ideal initial states.

Considering that the input pulse width $t_0 = 1$ ps is relatively narrow, higher-order effects may exist during propagation. Additionally, fiber loss is inevitable. To account for these factors, we conducted further numerical testing by considering third-order dispersion and fiber attenuation [49]. The physical model used for this testing is given by $i\Phi_{1,z} - \beta_2/2\Phi_{1,tt} - i\beta_3/6\Phi_{1,ttt} + \gamma(|\Phi_1|^2 + |\Phi_2|^2)\Phi_1 + i\alpha/2\Phi_1 = 0$ and $i\Phi_{2,z} - \beta_2/2\Phi_{2,tt} - i\beta_3/6\Phi_{1,ttt} + \gamma(|\Phi_1|^2 + |\Phi_2|^2)\Phi_2 + i\alpha/2\Phi_2 = 0$. β_3 and α represent the coefficients of third-order dispersion and attenuation, respectively. We have experimental parameters $\alpha = 0.25$ dB/km and $\beta_3 \approx 0.12$ ps^3/km [49]. Utilizing the dimensions defined above, the dimensionless coefficient of third-order dispersion is $\beta_3' = \beta_3/(6\beta_2 t_0) \approx 0.001$, and the dimensionless fiber loss is $\alpha' = \alpha z_0/2 \approx 0.0016$. The initial condition remains identical to that set in Figs. 4(b1) and 4(b2). The corresponding simulation results have been exhibited in Figs. 4(c1) and 4(c2), which almost align with the observations described in Figs. 4(a1) and 4(a2), 4(b1) and 4(b2), and 2(d). By utilizing the experimental setup described in Refs. [36,37], there is a high possibility of observing these RW excitations in real experiments. Therefore, by combining the phase diagrams and the resonance MI theory, there exist many more possibilities for observing various vector RWs in practical experiments.

V. CONCLUSION

In summary, the patterns of optical vector RWs in the defocusing regime have been systematically classified. We establish the equation correspondence between MI and exact RW solutions, which provides an important supplement for the results in the focusing regime [28,30]. We present the phase diagrams to illustrate the families of vector RW patterns in a two-component case, which can guide one to design appropriate resonance perturbations to observe them controllably in actual experiments. For example, we numerically demonstrate that the FP-FP patterns can be excited from a weak localized perturbation in two orthogonal polarization optical fibers. The results could be used to realize controllable RW pattern excitations in nonlinear coupled systems.

Note added. Recently, the authors became aware that the one-to-one correspondence between the baseband MI and the RW solutions was suggested in a different model [50].

ACKNOWLEDGMENTS

L.L. was supported by the National Natural Science Foundation of China (Grant No. 12122105). L.-C.Z. was sup-

ported by the National Natural Science Foundation of China (Contracts No. 12022513 and No. 11775176) and the Major Basic Research Program of Natural Science of Shaanxi Province (Grant No. 2018KJXX-094).

[1] D. H. Peregrine, Water waves, nonlinear Schrödinger equations and their solutions, J. Aust. Math. Soc. Ser. B **25**, 16 (1983).
[2] D. R. Solli, C. Ropers, P. Koonath, and B. Jalali, Optical rogue waves, Nature (London) **450**, 1054 (2007).
[3] B. Kibler, J. Fatome, C. Finot, G. Millot, F. Dias, G. Genty, N. Akhmediev, and J. M. Dudley, The Peregrine soliton in nonlinear fibre optics, Nat. Phys. **6**, 790 (2010).
[4] N. Akhmediev, J. M. Soto-Crespo, and A. Ankiewicz, Extreme waves that appear from nowhere: On the nature of rogue waves, Phys. Lett. A **373**, 2137 (2009).
[5] A. Chabchoub, N. P. Hoffmann, and N. Akhmediev, Rogue Wave Observation in a Water Wave Tank, Phys. Rev. Lett. **106**, 204502 (2011).
[6] H. Bailung, S. K. Sharma, and Y. Nakamura, Observation of Peregrine Solitons in a Multicomponent Plasma with Negative Ions, Phys. Rev. Lett. **107**, 255005 (2011).
[7] J. M. Dudley, G. Genty, A. Mussot, A. Chabchoub, and F. Dias, Rogue waves and analogies in optics and oceanography, Nat. Rev. Phys. **1**, 675 (2019).
[8] Yu. V. Bludov, V. V. Konotop, and N. Akhmediev, Matter rogue waves, Phys. Rev. A **80**, 033610 (2009).
[9] A. Romero-Ros, G. C. Katsimiga, S. I. Mistakidis, B. Prinari, G. Biondini, P. Schmelcher, and P. G. Kevrekidis, Theoretical and numerical evidence for the potential realization of the Peregrine soliton in repulsive two-component Bose-Einstein condensates, Phys. Rev. A **105**, 053306 (2022).
[10] Z. Yan, Vector financial rogue waves, Phys. Lett. A **375**, 4274 (2011).
[11] N. Akhmediev, A. Ankiewicz, and J. M. Soto-Crespo, Rogue waves and rational solutions of the nonlinear Schrödinger equation, Phys. Rev. E **80**, 026601 (2009).
[12] L. H. Wang, K. Porsezian, and J. S. He, Breather and rogue wave solutions of a generalized nonlinear Schrödinger equation, Phys. Rev. E **87**, 053202 (2013).
[13] B. Guo, L. Ling, and Q. P. Liu, Nonlinear Schrödinger equation: Generalized Darboux transformation and rogue wave solutions, Phys. Rev. E **85**, 026607 (2012).
[14] B.-L. Guo and L.-M. Ling, Rogue wave, breathers and bright-dark-rogue solutions for the coupled Schrödinger equations, Chin. Phys. Lett. **28**, 110202 (2011).
[15] F. Baronio, A. Degasperis, M. Conforti, and S. Wabnitz, Solutions of the Vector Nonlinear Schrödinger Equations: Evidence for Deterministic Rogue Waves, Phys. Rev. Lett. **109**, 044102 (2012).
[16] L.-C. Zhao and J. Liu, Localized nonlinear waves in a two-mode nonlinear fiber, J. Opt. Soc. Am. B **29**, 3119 (2012).
[17] L.-C. Zhao and J. Liu, Rogue-wave solutions of a three-component coupled nonlinear Schrödinger equation, Phys. Rev. E **87**, 013201 (2013).
[18] L.-C. Zhao, G.-G. Xin, and Z.-Y. Yang, Rogue-wave pattern transition induced by relative frequency, Phys. Rev. E **90**, 022918 (2014).
[19] C. Liu, S.-C. Chen, X. Yao, and N. Akhmediev, Non-degenerate multi-rogue waves and easy ways of their excitation, Phys. D **433**, 133192 (2022).
[20] J. S. He, H. R. Zhang, L. H. Wang, K. Porsezian, and A. S. Fokas, Generating mechanism for higher-order rogue waves, Phys. Rev. E **87**, 052914 (2013).
[21] L. Ling, B. Guo, and L.-C. Zhao, High-order rogue waves in vector nonlinear Schrödinger equations, Phys. Rev. E **89**, 041201(R) (2014).
[22] C. Liu, Z.-Y. Yang, L.-C. Zhao, G.-G. Xin, and W.-L. Yang, Optical rogue waves generated on Gaussian background beam, Opt. Lett. **39**, 1057 (2014).
[23] L.-C. Zhao, B. Guo, and L. Ling, High-order rogue wave solutions for the coupled nonlinear Schrödinger equations-II, J. Math. Phys. **57**, 043508 (2016).
[24] P. Gao, L.-C. Zhao, Z.-Y. Yang, X.-H. Li, and W.-L. Yang, High-order rogue waves excited from multi-Gaussian perturbations on a continuous wave, Opt. Lett. **45**, 2399 (2020).
[25] C. Kharif and E. Pelinovsky, Physical mechanisms of the rogue wave phenomenon, Eur. J. Mech. B **22**, 603 (2003).
[26] M. Onorato, S. Residori, U. Bortolozzo, A. Montina, and F. T. Arecchi, Rogue waves and their generating mechanisms in different physical contexts, Phys. Rep. **528**, 47 (2013).
[27] J. M. Dudley, F. Dias, M. Erkintalo, and G. Genty, Instabilities, breathers and rogue waves in optics, Nat. Photon. **8**, 755 (2014).
[28] L.-C. Zhao and L. Ling, Quantitative relations between modulational instability and several well-known nonlinear excitations, J. Opt. Soc. Am. B **33**, 2172 (2016).
[29] P. Gao, L. Duan, L.-C. Zhao, Z.-Y. Yang, and W.-L. Yang, Dynamics of perturbations at the critical points between modulation instability and stability regimes, Chaos **29**, 083112 (2019).
[30] L. Ling, L.-C. Zhao, Z.-Y. Yang, and B. Guo, Generation mechanisms of fundamental rogue wave spatial-temporal structure, Phys. Rev. E **96**, 022211 (2017).
[31] F. Baronio, M. Conforti, A. Degasperis, S. Lombardo, M. Onorato, and S. Wabnitz, Vector Rogue Waves and Baseband Modulation Instability in the Defocusing Regime, Phys. Rev. Lett. **113**, 034101 (2014).
[32] S. Chen, J. M. Soto-Crespo, and P. Grelu, Dark three-sister rogue waves in normally dispersive optical fibers with random birefringence, Opt. Express **22**, 27632 (2014).
[33] S. Chen, F. Baronio, J. M. Soto-Crespo, P. Grelu, and D. Mihalache, Versatile rogue waves in scalar, vector, and multi-dimensional nonlinear systems, J. Phys. A: Math. Theor. **50**, 463001 (2017).
[34] G. Zhang, Z. Yan, X.-Y. Wen, and Y. Chen, Interactions of localized wave structures and dynamics in the defocusing coupled nonlinear Schrödinger equations, Phys. Rev. E **95**, 042201 (2017).
[35] S. Chen, Y. Ye, J. M. Soto-Crespo, P. Grelu, and F. Baronio, Peregrine Solitons Beyond the Threefold Limit and Their Two-Soliton Interactions, Phys. Rev. Lett. **121**, 104101 (2018).

[36] B. Frisquet, B. Kibler, P. Morin, F. Baronio, M. Conforti, G. Millot, and S. Wabnitz, Optical dark rogue wave, Sci. Rep. **6**, 20785 (2016).

[37] F. Baronio, B. Frisquet, S. Chen, G. Millot, S. Wabnitz, and B. Kibler, Observation of a group of dark rogue waves in a telecommunication optical fiber, Phys. Rev. A **97**, 013852 (2018).

[38] F. Baronio, S. Chen, P. Grelu, S. Wabnitz, and M. Conforti, Baseband modulation instability as the origin of rogue waves, Phys. Rev. A **91**, 033804 (2015).

[39] F. T. Hioe, Solitary Waves for N Coupled Nonlinear Schrödinger Equations, Phys. Rev. Lett. **82**, 1152 (1999).

[40] G. P. Agrawal, *Nonlinear Fiber Optics* (Academic, New York, 1995).

[41] T. Kanna and M. Lakshmanan, Exact Soliton Solutions, Shape Changing Collisions, and Partially Coherent Solitons in Coupled Nonlinear Schrödinger Equations, Phys. Rev. Lett. **86**, 5043 (2001).

[42] A. I. Maimistov, Solitons in nonlinear optics, Quantum Electron. **40**, 756 (2010).

[43] N. Akhmediev, W. Królikowski, and A. W. Snyder, Artially Coherent Solitons of Variable Shape, Phys. Rev. Lett. **81**, 4632 (1998).

[44] L.-C. Zhao, L. Duan, P. Gao, and Z.-Y. Yang, Vector rogue waves on a double-plane wave background, Europhys. Lett. **125**, 40003 (2019).

[45] G. Biondini and D. Kraus, Inverse scattering transform for the defocusing Manakov system with nonzero boundary conditions, SIAM J. Math. Anal. **47**, 706 (2015).

[46] L. Ling, L.-C. Zhao, and B. Guo, Darboux transformation and multi-dark soliton for N-component nonlinear Schrödinger equations, Nonlinearity **28**, 3243 (2015).

[47] G. Biondini, E. Fagerstrom, and B. Prinari, Inverse scattering transform for the defocusing nonlinear Schrödinger equation with fully asymmetric non-zero boundary conditions, Phys. D **333**, 117 (2016).

[48] B. Frisquet, B. Kibler, J. Fatome, P. Morin, F. Baronio, M. Conforti, G. Millot, and S. Wabnitz, Polarization modulation instability in a Manakov fiber system, Phys. Rev. A **92**, 053854 (2015).

[49] M. Droques, B. Barviau, A. Kudlinski, M. Taki, A. Boucon, T. Sylvestre, and A. Mussot, Symmetry-breaking dynamics of the modulational instability spectrum, Opt. Lett. **36**, 1359 (2011).

[50] S. Chen, L. Bu, C. Pan, C. Hou, F. Baronio, P. Grelu, and N. Akhmediev, Modulation instability-rogue wave correspondence hidden in integrable systems, Commun. Phys. **5**, 297 (2022).